AIAA JOURNAL
Vol. 48, No. 2, February 2010

Prediction of Sound Generated by Complex Flows at Low Mach Numbers

Yaser Khalighi,* Ali Mani,* Frank Ham,† and Parviz Moin‡
Stanford University, Stanford, California 94305

DOI: 10.2514/1.42583

We present a computational aeroacoustics method to evaluate sound generated by low Mach number flows in complex configurations in which turbulence interacts with arbitrarily shaped solid objects. This hybrid approach is based on Lighthill's acoustic analogy in conjunction with sound source information from an incompressible calculation. In this method, Lighthill's equation is solved using a boundary element method that allows the effect of scattered sound from arbitrarily shaped solid objects to be incorporated. We present validation studies for sound generated by laminar and turbulent flows over a circular cylinder at $Re = 100$ and 10,000, respectively. Our hybrid approach is validated against directly computed sound using a high-order compressible flow solver as well as the solution of the Ffowcs Williams and Hawkings equation in conjunction with compressible sound sources. We demonstrate that the sound predicted by a second-order hybrid approach is as accurate as sound directly computed by a sixth-order compressible flow solver in the frequency range in which low-order numerics can accurately resolve the flow structures. As an example of an engineering problem, we calculated the sound generated by flow over an automobile side-view mirror and compared it to experimental measurements.

Nomenclature

C_D, C_L	=	drag and lift coefficients, respectively
c	=	speed of sound
d	=	dimension of the problem
e_{ij}	=	viscous stress tensor
f	=	frequency
G	=	Green's function of the Helmholtz operator
k	=	wave number
L, L_c	=	width of the mirror, recirculation length
M, M_i	=	freestream Mach number, freestream vector Mach number
n_i	=	unit outward to the boundary $\partial\Omega$
p, p_a	=	pressure, acoustic pressure defined as $c_0^2\rho'$
Re	=	Reynolds number
r	=	distance from the sound source region
St	=	Strouhal number
T_{ij}	=	Lighthill's stress tensor
t	=	time
$\mathbf{u}$, $\mathbf{v}$	=	compressible and incompressible velocities, respectively
u	=	streamwise velocity
$\mathbf{x}$, $\mathbf{y}$	=	locations of the observer and the source, respectively
x_i	=	Cartesian coordinate
α	=	domain-dependent geometrical factor
δ_{ij}	=	Kronecker delta
ρ	=	fluid density
Φ	=	power spectral density
Ω, $\partial\Omega$	=	acoustic medium, boundary of the acoustic medium, that is, solid boundary
$\Omega\backslash\{\mathbf{x}\}$	=	domain Ω excluding the point $\mathbf{x}$
ω	=	angular frequency
$\|$	=	modulus of a complex quantity
$[]_{\mathbf{x}}$	=	quantity evaluated at observer location $\mathbf{x}$

Subscript

0	=	reference quantity

Superscripts

$'$	=	difference from the reference quantity
$\sim$	=	quantity in the frequency domain
$-$	=	time mean of the quantity
rms	=	rms. of the quantity

I. Introduction

IN MANY practical applications, sound is generated by the interaction of turbulent flow with solid objects. Here, sound waves experience multiple reflections from solid objects before they propagate to an observer. To predict the acoustic field in such situations requires a general aeroacoustic framework to operate in complex environments. Furthermore, the method employed must avoid making simplifying assumptions about the geometry, compactness, or frequency content of sound sources. The present work aims to develop, validate, and demonstrate the functionality of such a computational framework.

The prediction of flow-generated sound must account for the physics of both unsteady flow and sound simultaneously. Because these two phenomena exhibit very different energy and length scales, prediction of flow-generated sound is challenging, especially from a numerical perspective. Sound waves carry only a minuscule fraction of flow energy, and accurate numerical schemes with low dissipation and low dispersion are required in a direct computation to keep the sound waves intact. Additionally, in the low Mach number regime, the acoustic Courant-Friedrichs–Lewy (CFL) number imposes extremely small time steps on numerics for resolving both acoustics and hydrodynamics. To avoid such computational difficulties, various hybrid approaches have employed Lighthill's acoustic analogy [1], which allows for the use of separate numerics suited to each physical phenomenon. In particular, at low Mach numbers, the unsteady hydrodynamic field is computed by an incompressible flow solver in which the time step is not restricted by the acoustic CFL number. This solution is then used to represent the sound sources in a separate acoustic solver.

Received 16 December 2008; revision received 21 September 2009; accepted for publication 18 October 2009.

*Graduate Student, Department of Mechanical Engineering, Center for Turbulence Research.
†Research Associate, Center for Turbulence Research.
‡Franklin and Caroline Johnson Professor on Engineering, Department of Mechanical Engineering. Fellow AIAA.

Curle demonstrated that the presence of solid bodies significantly increases the efficiency of sound emission at low Mach numbers [2]. Thus, special care is needed to calculate the sound generated by the interaction of flow and solid objects. One way of treating the scattering from solid objects is to employ geometry-tailored Green's functions in the integral solution to Lighthill's equation. Analytical methods have been extensively used to calculate trailing-edge noise. In several studies [3–5], analytical Green's functions obtained by Ffowcs Williams and Hall [6] and Howe [7] have been employed in conjunction with the incompressible large eddy simulation (LES) to calculate the sound generated by turbulent flows over trailing edges. This approach, however, is limited to scattering from simple geometries for which Green's function can be derived analytically. For complex geometries, the exact Green's function must be obtained numerically. A boundary element method (BEM) is applied in several studies [8–10] to compute the exact Green's function in calculating flow-generated sound. This numerical technique is particularly attractive for exterior acoustic problems as it naturally satisfies the causality condition in the far field; in addition, it is not subject to dispersion and dissipation errors in contrast to methods using finite difference, finite volume, and finite element. The main drawback to this approach, however, is that Green's functions depend on the location of the observer; accordingly, to study the sound directivity or sound spectra for numerous observers, evaluation of the geometry-tailored Green's function as well as the volume integrals in Lighthill's equation can be computationally intensive.

Alternatively, scattering of sound can be traced numerically by solving the linear acoustic equation with proper boundary conditions. For example, Oberai et al. [11] used the finite element method to solve Lighthill's equation to calculate trailing-edge noise. The difficulty inherent in such approaches is that, for unbounded domains, extra treatments such as Dirichlet to Neumann [12], perfectly matched layer [13], or infinite elements [14] are required to avoid the reflection of sound from exterior boundaries. In addition, for a far-field observer, either the computational domain must be extended to include the observer's location or an acoustic projection method such as Kirchhoff's surface must be applied. These difficulties can be avoided by using BEM. Hence, in the present work, BEM is used to directly solve Lighthill's equation.

We introduce an aeroacoustic solver that can operate in an arbitrarily complex geometry environment. In this hybrid approach, the flow-generated sound sources are computed using the low-dissipation unstructured incompressible LES solver of Ham and Iaccarino [15]. These sources are then used as the input to an acoustic solver, in which Lighthill's equation with convection effects is transformed to a boundary integral equation and solved using a BEM scheme introduced by Khalighi and Bodony [16]. The key features of this new approach are listed as follows:

1) This method has no limitations other than the low Mach number assumption and intrinsic limitation of Lighthill's theory with incompressible sources described by Crow [17]. This formulation is valid for the entire frequency range, and no source/body compactness assumption is made, in contrast to the work of Schram [18], in which the compactness of the source is assumed. Another distinction between our approach and Schram's is that, in Schram, the pressure is decomposed into acoustics and hydrodynamics; volume-distributed source terms are also split into near- and far-field regions; there are no such decompositions in the present work.

2) The effect of uniform background convection is fully included in the formulation, whereas it is neglected in almost all previous BEM-based approaches (for exceptions, see [10,19,20]).

3) Numerical differentiations of sound sources are avoided. According to Crighton [21], the error caused by such differentiations can overwhelm the real sound in the limit of small Mach number.

4) In contrast to the BEM-based approaches that evaluate the exact Green's function [8–10], in our proposed method, numerical evaluation of the derivatives of Green's functions is not required. Furthermore, sound can be evaluated for multiple observers at little computational cost.

The paper is organized as follows. We first derive the boundary integral equations and introduce the structure of the hybrid approach. Then, we present studies validating this method for canonical problems of sound generation by laminar and turbulent flows over a cylinder. Finally, we demonstrate the method's applicability to engineering problems by computing the sound generated by flow around an automotive side-view mirror and provide a detailed comparison with the experimental data.

II. Methodology

Figure 1 describes the physical setting in which an acoustic analogy is used. Sound waves are generated by unsteady flow and travel to the observer either directly or after reflections from hard walls. Based on this physical picture, in Lighthill's analogy the compressible Navier–Stokes equations are rearranged into an inhomogeneous wave equation for density ρ with flow quantities as source terms [1]. Moving the convection effects from the right-hand side and including them in the wave operator yields

$$\left(\frac{D^2}{Dt^2} - c_0^2 \frac{\partial^2}{\partial x_j \partial x_j}\right)\rho' = \frac{\partial^2 T'_{ij}}{\partial x_i \partial x_j} \quad [\Omega] \tag{1}$$

In Eq. (1), c_0 is the reference speed of sound, and $\frac{\mathrm{D}}{\mathrm{D}t} \equiv \frac{\partial}{\partial t} + U_i \frac{\partial}{\partial x_i}$ is the material time derivative. The sound source term T'_{ij} is written in terms of flow quantities as

$$T'_{ij} = \rho u'_i u'_j - e_{ij} + \delta_{ij}(p' - c_0^2 \rho') \tag{2}$$

where $u'_i = u_i - U_i$ are velocity components with background convection subtracted, e_{ij} is the viscous stress, $p' = p - p_0$ and $\rho' = \rho - \rho_0$. The subscript 0 denotes the reference quantities. We take the temporal Fourier transform of Eq. (1) and arrive at the following equation:

$$\left(\left(ik + M_i \frac{\partial}{\partial x_i}\right)^2 - \frac{\partial^2}{\partial x_j \partial x_j}\right)\tilde{p}'_a = \frac{\partial^2 \tilde{T}'_{ij}}{\partial x_i \partial x_j} \quad [\Omega] \tag{3}$$

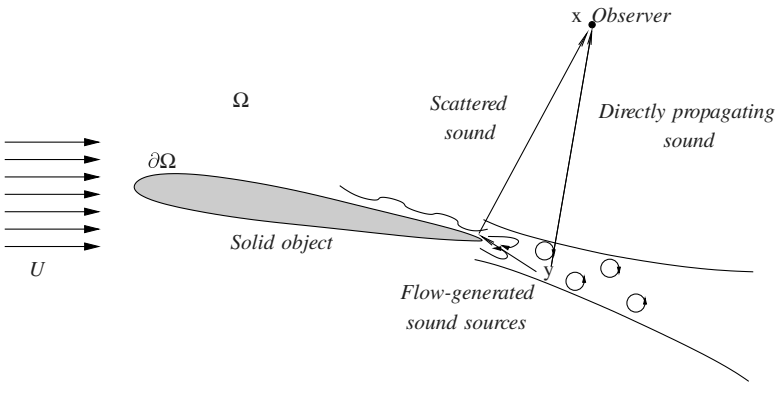

Fig. 1 Schematic of sound generation and propagation by flow over a generic solid object.

where $\sim$ denotes Fourier-transformed quantities, $p'_a = \rho' c_0^2$ is the acoustic pressure, $M_i = U_i/c_0$, and $k = \omega/c_0$.

Equation (3) is subject to hard-wall boundary conditions on solid walls $\partial\Omega$ and the Sommerfeld condition in the far field. In the Appendix, we use these boundary conditions and apply Green's identities to transform Eq. (3) to the following boundary integral equation:

$$[\alpha(\tilde{p}'_a + A_{ij}\tilde{T}'_{ij})]_{\mathbf{x}} = -\int_{\partial\Omega\setminus\{\mathbf{x}\}} [((\delta_{ij} - M_i M_j)\widetilde{p'_a} + \tilde{T}'_{ij})n_j]_{\mathbf{y}} \frac{\partial G(\mathbf{x}|\mathbf{y})}{\partial y_i} \mathrm{d}s_y + \int_{\Omega\setminus\{\mathbf{x}\}} \tilde{T}'_{ij}(\mathbf{y}) \frac{\partial^2 G(\mathbf{x}|\mathbf{y})}{\partial y_i \partial y_j} \mathrm{d}\mathbf{y} \tag{4}$$

In Eq. (4), $G(\mathbf{x}|\mathbf{y})$ is the free-space Green's function of the "convective" Helmholtz operator appearing on the left-hand side of Eq. (3); $\mathbf{y}$ and $\mathbf{x}$ are the locations of the source and observer, respectively. The analytical representation of $G(\mathbf{x}|\mathbf{y})$ is given in the Appendix. α is a geometrical factor and A_{ij} is a diagonal matrix defined in the Appendix. At low Mach numbers, $A_{ij} = 1/d + O(M^2)$, where d is the dimension of the problem.

Equation (4) is an exact rearrangement of compressible Navier–Stokes equations. Although the purpose of this rearrangement is to extract the acoustic pressure p'_a that represents acoustic waves in the far field, the source term T'_{ij} is dependent on compressible effects because it includes compressible velocity, density, and pressure. According to Lighthill [1], in the limit of low Mach number, for nonheated and nonreacting application, this term can be approximated using incompressible sources as $T'_{ij} \approx \rho_0 v'_i v'_j$ with $v'_i = v_i - U_i$, where v_i is taken to be the incompressible velocity field (for a discussion on the adequacy of this approximation, see [17]). The viscous effect is known to contribute little to Lighthill's stress tensor. In particular, having evaluated the viscous term by the incompressible solution, that is, $e_{ij} \approx e^0_{ij} = \mu_0(\frac{\partial v_i}{\partial x_j} + \frac{\partial v_j}{\partial x_i})$, the double divergence of e^0_{ij} is identically zero and does not appear as a sound source term. However, the shear viscous stress is required to satisfy the no-penetration boundary condition on the solid surfaces and cannot be discarded; this requirement is consistent with the conclusion of Shariff and Wang [22]. Consequently, the viscous term is included in the surface integrals and neglected as a volume source term. According to the above discussion, for low Mach number flows, Eq. (4) is written as

$$\begin{aligned}[\alpha(\tilde{p}'_a + \rho_0\widetilde{v'_i v'_i}/d)]_{\mathbf{x}} &= -\int_{\partial\Omega\setminus\{\mathbf{x}\}} [((\delta_{ij} - M_i M_j)\tilde{p}'_a)n_j]_{\mathbf{y}} \frac{\partial G(\mathbf{x}|\mathbf{y})}{\partial y_i}\, \mathrm{d}s_y \quad \text{scattered} \\ &+ \int_{\Omega\setminus\{\mathbf{x}\}} [\rho_0\widetilde{v'_i v'_j}]_{\mathbf{y}} \frac{\partial^2 G(\mathbf{x}|\mathbf{y})}{\partial y_i \partial y_j}\, \mathrm{d}\mathbf{y} \quad \text{direct} \\ &+ \int_{\partial\Omega\setminus\{\mathbf{x}\}} [\tilde{e}^0_{ij} n_j]_{\mathbf{y}} \frac{\partial G(\mathbf{x}|\mathbf{y})}{\partial y_i}\, \mathrm{d}s_y \quad \text{viscous}\end{aligned} \tag{5}$$

After the $\rho_0 v'_i v'_j$ and e^0_{ij} terms are computed using an incompressible solver, pressure $\tilde{p}'_a$ remains the only unknown variable in Eq. (5). This equation is at the core of the hybrid approach. Figure 2, which shows the structure of the hybrid approach, describes the process of calculating sound at an observer location $\mathbf{x}$ using Eq. (5). We use an incompressible flow solver to compute flow-generated sound sources. This is a second-order, low-dissipation, unstructured, finite volume LES solver based on the numerical scheme of Ham and Iaccarino [15]. This solver is specialized for high-quality and large-scale calculations of multiscale/multiphysics problems and has been successfully tested in a variety of applications (for more information about this solver, see [23]). Using the incompressible solution, we calculate the Fourier modes of $\rho_0\widetilde{v'_i v'_j}$ and $\tilde{e}^0_{ij}$; then, for each frequency we substitute these terms in Eq. (5) and solve it for pressure $\tilde{p}'_a$ in the following two-step approach:

1) Solving for $\tilde{p}'_a$ on $\partial\Omega$: Calculating pressure $\tilde{p}'_a$ in Eq. (5) requires solution of Fredholm's integral equation of the second kind. Therefore, we start by taking the first integral to the left-hand side of Eq. (5), then discretize the integral by meshing the boundary $\partial\Omega$ and using a surface quadrature rule. We employ the BEM introduced in [24] to form a well-conditioned linear system of equations. To calculate the right-hand side of this system of equations, we place the observer point $\mathbf{x}$ at the centroid of each facet and evaluate the second and third integrals in Eq. (5). This is equivalent to propagating the sound waves directly to the solid surface. To obtain $\tilde{p}'_a$ on $\partial\Omega$, this linear system is solved using a parallel direct solver [25].

2) Integrating for $\tilde{p}'_a$ at the observer point $\mathbf{x}$: After pressure $\tilde{p}'_a$ on $\partial\Omega$ is computed, we simply use surface and volume quadratures to integrate the right-hand side of Eq. (5) and calculate the total sound at any observer point.

For numerical evaluation of the surface and volume integrals in the above procedure, p'_a, e^0_{ij}, and $\rho_0 v'_i v'_j$ are assumed to be constant within each surface or volume element. Because of the singularity of integral kernels, that is, free-space Green's functions, a piecewise constant representation of these kernels leads to an erroneous evaluation of integrals. To resolve this discrepancy, these kernels are approximated by the corresponding asymptotic behavior in the vicinity of the singular region; these singular functions are then used for analytical evaluation of the integrals (for more detail about this procedure, see [16]).

According to Eq. (5), sound evaluated in the hybrid approach has three components: *scattered*, *direct*, and *viscous*. The direct and scattered components are depicted in Fig. 1; the portion of sound that travels to the observer without encountering the solid object corresponds to the direct sound, whereas the portion that encounters the solid object contributes to the scattered sound. The viscous term (which can be interpreted as a scattering effect [26]) is often small; among all of the test cases studied in the present work, this effect was appreciable only in the problem of laminar vortex shedding from a cylinder.

It should be emphasized that both acoustics and hydrodynamics contribute to the pressure in the hybrid approach; however, in the near field (particularly on the solid surface), this pressure is almost entirely due to hydrodynamic effects; furthermore, a dimensional analysis (similar to the analysis of Curle [2]) shows that, at low frequencies where both the source region and solid object are compact, the scattered surface term dominates the far-field sound. Consequently, at low frequencies, Eq. (5) can be simplified to

$$\tilde{p}'_a(\mathbf{x}) \approx -\int_{\partial\Omega} [((\delta_{ij} - M_i M_j)\tilde{p}_{\mathrm{hyd}})n_j]_{\mathbf{y}} \frac{\partial G(\mathbf{x}|\mathbf{y})}{\partial y_i}\, \mathrm{d}s_y \tag{6}$$

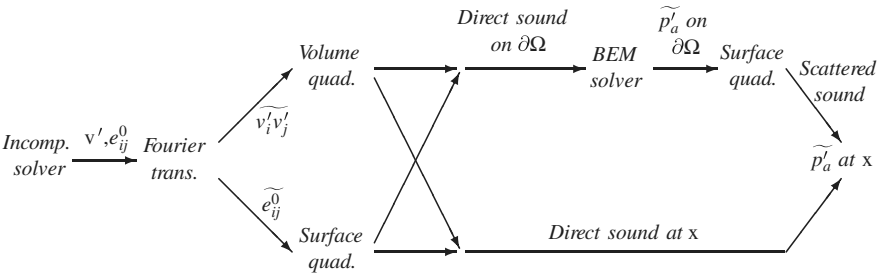

Fig. 2 Flowchart showing the structure of the hybrid approach.

where p_{hyd} is the hydrodynamic pressure obtained from the incompressible simulation. Because of its simplicity, this approach is widely used in commercial software. It produces accurate results only in the low-frequency range and underpredicts the sound at higher frequencies where the source region and the solid body are not compact. This property will be demonstrated in the study of sound generated by turbulent flow over a cylinder (see Sec. III.B).

III. Validation

The sound calculated by the hybrid approach is validated against the density fluctuations directly computed using a high-order compressible flow solver as well as sound calculated by the Ffowcs Williams and Hawkings (FW-H) formulation [27] based on the compressible solution. For the compressible calculations we applied the staggered sixth-order finite difference scheme of Nagarajan et al. [28] and customized it for sound calculation. Specifically, a sponge layer was carefully designed to avoid reflection or generation of spurious sound from the exterior boundary. The details of the sponge layer will be given for each case. For the FW-H method, the control surface is fixed to the surface of the solid object; to account for the sound generated outside of this control surface, the quadrupolar volume integral is included in the FW-H calculations.

Given that the accuracy of calculated sound closely depends on the flow solution, our study included the near-field hydrodynamics in addition to the sound in all test cases presented here. Validation studies were carried out for canonical problems of sound generated by laminar and turbulent flow over a cylinder. The identical near-field resolution, run time, and sampling rate were used for compressible and incompressible simulations.

A. Sound Generated by Laminar Flow over a Cylinder

Laminar vortex shedding from a cylinder at $Re = 100$ and $M = 0.15$ is considered. The computational domain for this flow configuration is shown in Fig. 3. At this Reynolds number, the flow is two-dimensional and can be entirely resolved on the computational grid. The mesh size is 300×300 in the wall-normal and azimuthal directions; the mesh is extended 28 diameters downstream of the cylinder. After achieving a steady state, simulation is advanced for 20 shedding cycles. The nondimensional numerical time step for the incompressible calculation in the hybrid method is $\Delta t U_0/D = 7.56 \times 10^{-3}$, where D and U_0 are the diameter of the cylinder and the freestream velocity, respectively. The time step for the compressible calculations is smaller owing to acoustic stiffness. The time step for the direct method is 4.91×10^{-4}.

The Strouhal number of shedding was the same in all simulations and equal to 0.165, which is in agreement with the study of Fey et al. [29]. A comparison of mean velocity in Fig. 4 shows excellent agreement with near-field hydrodynamics.

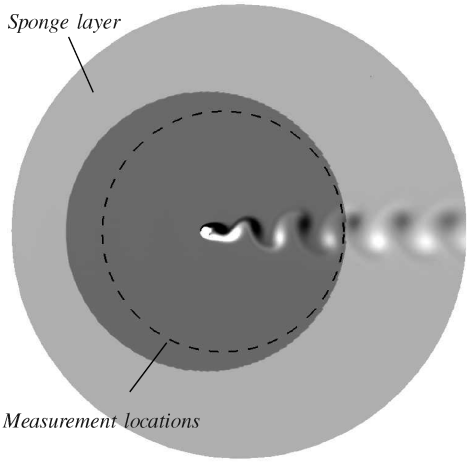

Fig. 3 Vorticity contour plot of laminar vortex shedding from cylinder at $Re = 100$. The measurement locations and the sponge layer are shown in the hybrid approach.

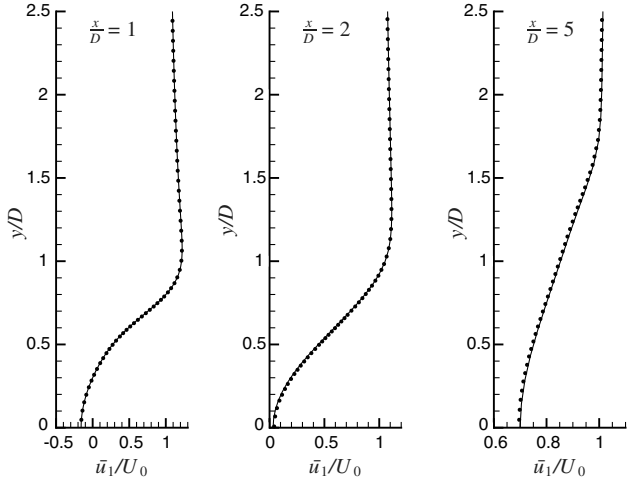

Fig. 4 $\bar{u_1}/U_0$ for three stations in the wake of the cylinder; solid line, compressible; dot, incompressible.

Silently traveling vortices can generate nonphysical sound when they exit the computational domain [30]. To prevent this, the velocity field is "silently" damped in a sponge layer, shown in Fig. 3. The damping function by which the velocity components are multiplied is

$$S(r) = \exp(-2.28\xi^3 - 6.21\xi^{11})$$
$$\text{where } \xi = \max\left(\frac{r - r_{\min}}{r_{\max} - r_{\min}}, 0\right)$$
$$r_{\min} = 14.0D, \qquad r_{\max} = 24.36D \tag{7}$$

where r is the radial distance from a point located $1.5D$ downstream of the cylinder. To design the sponge layer, a silently traveling vortex is considered; the damping function $S(r)$ is designed such that it does not generate significant amounts of spurious sound by damping this vortex.

The sponge treatment is applied in the hybrid approach to damp the source terms after the incompressible simulation is carried out. However, in the compressible calculation, the sponge is actively applied as a damping term during the simulation to absorb the outgoing acoustic waves. For more details about the analysis and applications of nonreflecting boundary conditions, see the work of Bodony [31].

In the compressible simulation, far-field sound is directly measured by sampling the density signal at measurement locations, shown in Fig. 3. These measurement points are not centered with respect to the cylinder. Instead, they are located on a circle centered 1.86 diameters downstream of the cylinder, with a radius of 12.9 diameters. This circle coincides with the front of a propagating and convecting sound wave generated at the cylinder. A comparison of sound computed from compressible and the hybrid approaches is presented in Fig. 5. In this figure the directivity pattern of sound is plotted for the shedding frequency f_{sh} and its first three harmonics. For each frequency, the relative sound pressure level (SPL) is reported in decibels. This quantity is defined as

$$\text{SPL} = 20 \log \frac{\max(|\tilde{p}'_a|)}{\max(|\tilde{p}'_{a0}|)} \tag{8}$$

where $|\tilde{p}'_{a0}|$ is the modulus of pressure mode at the shedding frequency.

Figure 5 demonstrates an excellent agreement between the directly computed sound, the result of the FW-H method, and the result of the hybrid approach at the shedding frequency and its first three harmonics. This agreement is most remarkable at $f = 4f_{sh}$, where the relative loudness level is substantially small.

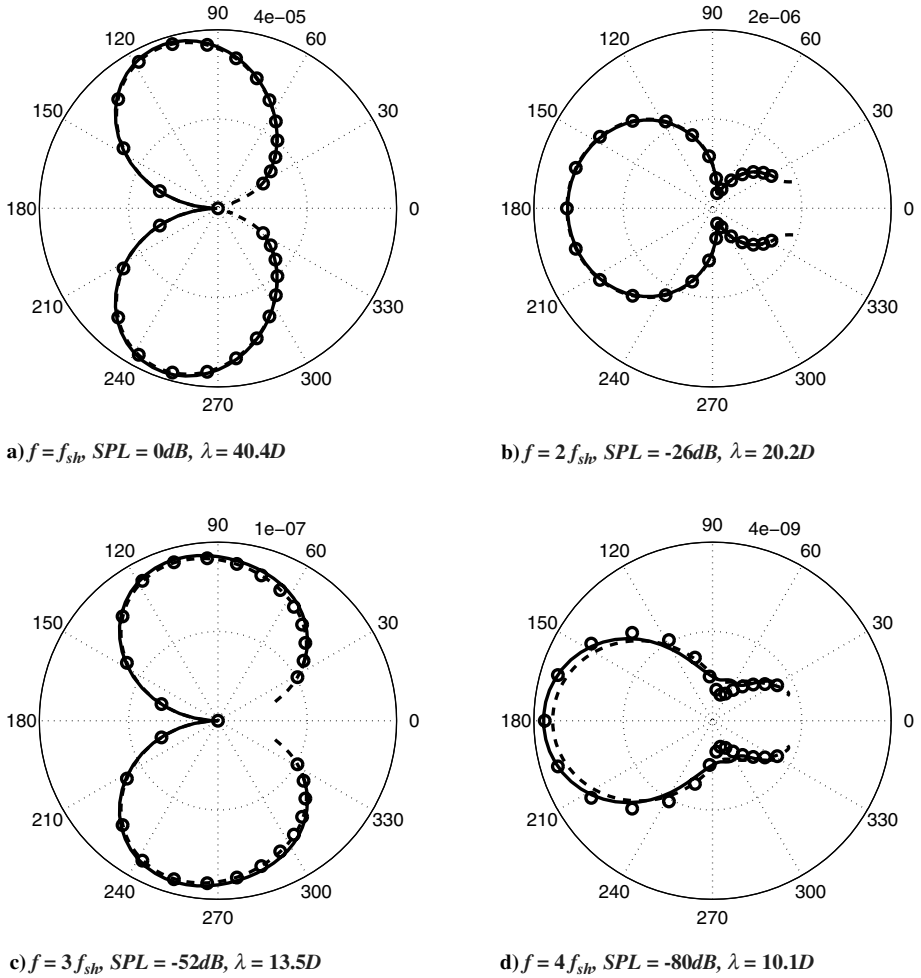

a) $f = f_{sh}$, $SPL = 0dB$, $\lambda = 40.4D$ **b)** $f = 2f_{sh}$, $SPL = -26dB$, $\lambda = 20.2D$

c) $f = 3f_{sh}$, $SPL = -52dB$, $\lambda = 13.5D$ **d)** $f = 4f_{sh}$, $SPL = -80dB$, $\lambda = 10.1D$

Fig. 5 Directivity plot of sound; solid line, hybrid approach; dashed line, directly computed sound; circle, FW-H based on compressible solution.

B. Sound Generated by Turbulent Flow over a Cylinder

We consider turbulent flow over a cylinder at $Re = 10,000$ and $M = 0.2$ as the second test case for validating the hybrid approach. At this Reynolds number, the flow in the wake is turbulent and LES with the dynamic Smagorinsky model is employed to account for subgrid scales [32]. The flow is three dimensional, and we used periodic boundary conditions in the spanwise direction for both compressible and incompressible simulations. The mesh size is $576 \times 320 \times 48$ in the wall-normal, azimuthal, and spanwise directions. The spanwise size of computational domain is chosen to be πD, where D is the diameter of the cylinder; the domain is extended $54D$ downstream of the cylinder. After the initial transient phase, both simulations are advanced for 80 shedding cycles. The nondimensional time step for these calculations is $\Delta U0/D = 4.125 \times 10^{-3}$. Similar to the laminar cylinder, a sponge zone with the following profile is applied to damp the velocity components:

$$S(r) = \exp(-5.72\xi^3 - 15.6\xi^{11}),$$
$$\text{where } \xi = \max\left(\frac{r - r_{\min}}{r_{\max} - r_{\min}}, 0\right), \tag{9}$$
$$r_{\min} = 21.0D, \qquad r_{\max} = 45.5D$$

where r is the radial distance from a point located $9.0D$ downstream of the cylinder.

A flow snapshot is shown in Fig. 6. In this picture, obtained from the compressible simulation, the vortical flow structures as well as sound waves are visualized. Clearly, sound waves are mostly generated in the vicinity of the cylinder, and their length scale is much larger than the flow length scales.

We compared the near-field hydrodynamics by studying first- and second-order flow statistics. Mean and rms velocity profiles in the wake of the cylinder are plotted in Fig. 7. These results show good agreement between the compressible and incompressible solutions. Table 1 summarizes the values of the global flow statistics measured in both simulations. For validation purposes, we also provided measures of statistical uncertainty in our results, because this flow has a slow time scale of the order of 10 shedding cycles and, depending on the time window chosen for averaging, the calculated averaged quantity can vary significantly. To evaluate the statistical uncertainty in quantities presented in Table 1, we divided the sample into five equal intervals and calculated those quantities in each interval; assuming that these five realizations are uncorrelated, the statistical error for each quantity is estimated based on a 95%

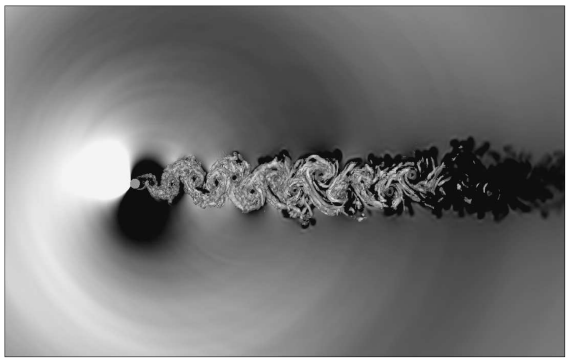

Fig. 6 Instantaneous vorticity isosurfaces in the wake shown over the density contour plot for flow over a cylinder at $Re = 10,000$.

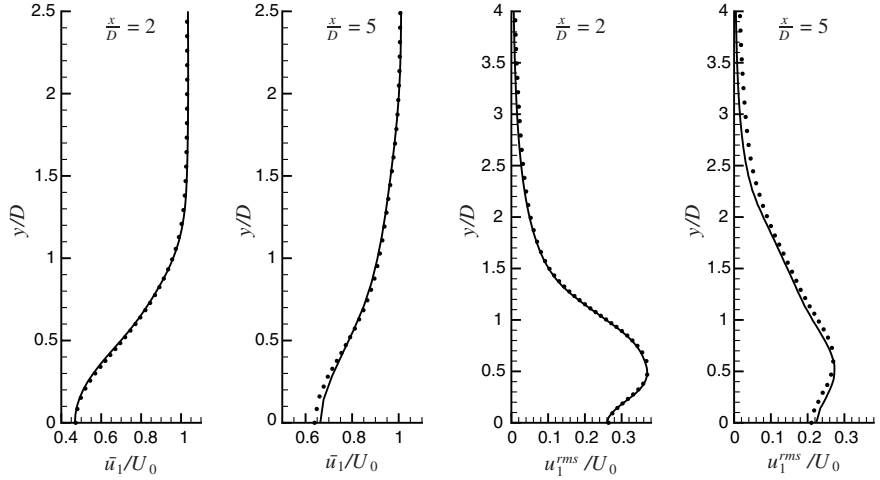

Fig. 7 $\bar{u_1}/U_0$ and u_1^{rms}/U_0 for two stations in the wake of the cylinder; solid line, compressible; dot, incompressible.

confidence interval (for the recirculation length, the statistical error is approximated based on two intervals). The relatively high uncertainty bounds in some quantities such as C_D^{rms} suggest that simulations should be advanced for a much longer time to obtain more accurate estimates. In light of the statistical uncertainty, the results of Table 1 demonstrate reasonable agreement between compressible and incompressible calculations.

The spectra of two diagonal elements of T'_{ij}, that is, $u'_1u'_1$ and $u'_2u'_2$, at a pair of points located $5D$ and $15D$ downstream of the cylinder, are shown in Fig. 8. Clearly, the spectra obtained from the compressible solution are more energetic at high frequencies owing to the difference between the numerical methods. The sixth-order, staggered numerical scheme of the compressible solver resolves higher wave numbers better than the second-order, collocated scheme of the incompressible code. Furthermore, the agreement between the two solutions extends to higher frequencies at the location of probe A; this agreement is attributed to the higher mesh resolution at the location of probe A. Also, the agreement in the latitudinal component of T'_{ij}, that is, $u'_2u'_2$, extends to higher frequencies compared to the longitudinal component of T'_{ij}.

Figure 9 shows the sound pressure spectra for two observers located approximately 16 diameters above the cylinder and 13.5 diameters upstream of the cylinder. To improve the statistical convergence, these spectra are first octave bin averaged where every octave is divided into six logarithmically equally spaced frequency bands. In addition, for the observer located above the cylinder, we benefit from the symmetry of the problem by averaging the spectra in the upper and lower sides of the cylinder.

A comparison of the directly computed sound and the result of the hybrid approach demonstrates that the sound pressure spectra follow the same trend as the sound source spectra: the results are in good agreement in the low- and intermediate-frequency range, whereas at high frequencies the sound calculated from the hybrid approach contains less energy.

In addition to the hybrid and direct methods, we applied the FW-H method to calculate the sound. According to Fig. 9, the FW-H solution is in excellent agreement with the directly computed sound, due to the fact that the FW-H method uses the compressible solution as the source term; thus, the sound computed based on this approach has the same energy content as the directly computed sound.

We also applied Eq. (6) to calculate the sound, using the surface pressure obtained from the incompressible simulation. Figure 9 clearly demonstrates that this method produces accurate results only in the low-frequency range and significantly underpredicts the sound at higher frequencies. This underprediction is mostly due to discarding the quadrupolar volume term.

Figure 10 shows the directivity of sound at four frequencies. The measurement points are located on a circle centered 3.26 diameters downstream of the cylinder with the radius of 16.8 diameters. We applied the same averaging techniques as those used in calculating the spectra, that is, one-sixth octave band bin averaging and symmetry averaging. Note that these directivity plots show the energy levels in linear scale; consequently, the difference between the various approaches is more noticeable in these figures than in Fig. 9, in which the spectra are presented in logarithmic scale.

The small difference between the directly computed sound and the result of the hybrid approach at $f = f_{\text{sh}}$ and $2f_{\text{sh}}$ is attributed to statistical uncertainty; the sound field at these frequencies is dominated largely by oscillating lift and drag forces on the cylinder and, based on the statistical error bounds reported in Table 1, the uncertainty in these quantities can be as large as 15%. The larger difference observed at $f = 4f_{\text{sh}}$ and $8f_{\text{sh}}$ is caused by the discrepancy in the energy content of the sound sources; Fig. 8 shows that, at high frequencies, the T_{ij} spectra calculated by the low-order incompressible solver diverge from the compressible solution calculated by the high-order solver. At midfrequencies, in particular $f = 4f_{\text{sh}}$, Fig. 8 demonstrates good agreement between the two solutions in the latitudinal component of T'_{ij}; however, for the longitudinal component of T'_{ij} the incompressible solution contains less energy. This difference can explain the partial disagreement in the directivity plot observed at larger angles for $f = 4f_{\text{sh}}$.

As observed earlier, very good agreement between the direct computation and FW-H analogy is obtained at all frequencies, and the application of Eq. (6) leads to substantial underprediction of sound at high frequencies.

Table 1 Comparison of shedding frequency St, mean drag coefficient $\bar{C}_D$, rms drag coefficient C_D^{rms}, rms lift coefficient C_L^{rms}, and recirculation length L_c

	Incompressible	Compressible
St	0.196 ± 0.003	0.192 ± 0.005
$\bar{C}_D$	1.27 ± 0.03	1.29 ± 0.06
C_D^{rms}	0.091 ± 0.013	0.098 ± 0.01
C_L^{rms}	0.61 ± 0.05	0.63 ± 0.09
L_c/D	0.69 ± 0.06	0.68 ± 0.01

IV. Sound Generated by Flow over an Automobile Side-View Mirror

In this section we apply the hybrid method to the computation of sound generated by flow over an automobile side-view mirror. Given the freestream velocity of 22.4 m/s (50.0 mph) and the mirror width of 20 cm, the Reynolds number is approximately equal to 300,000. Experimental measurements for flow over this bluff body, flush mounted on a test table, were conducted at the anechoic chamber facility at the University of Notre Dame [33] and the wind-tunnel facilities of the Institute for Aerospace Research at the National Research Consortium Canada [34]. Particle image velocimetry (PIV)

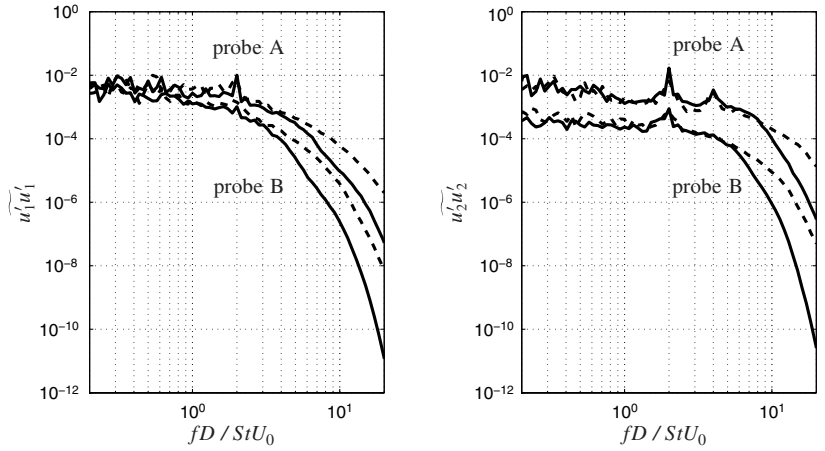

Fig. 8 Spectral density of three components of Lighthill's stress tensor at probe A located at $(5D, 0)$ and probe B located at $(15D, 0)$; solid line, incompressible; dashed line, compressible.

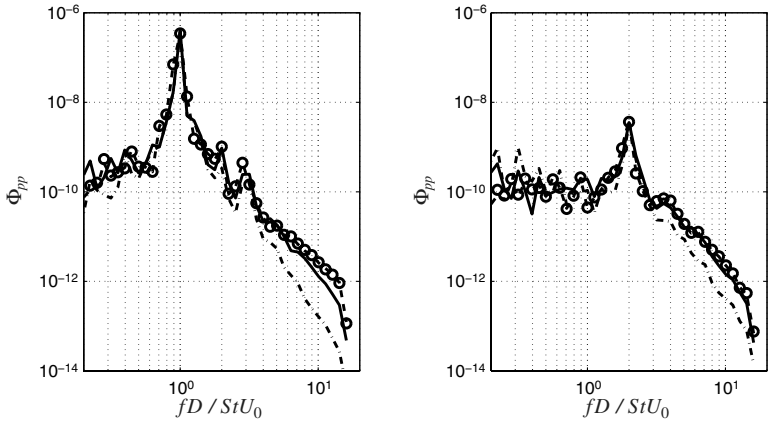

a) Observer at $(-1.2D, 16.2D)$ **b) Observer at $(-13.5D, 0)$**

Fig. 9 Spectral density of sound; solid line, hybrid approach; dashed line, directly computed sound; circle, FW-H based on compressible solution; dashed-dotted line, projection of hydrodynamic surface pressure using Eq. (6).

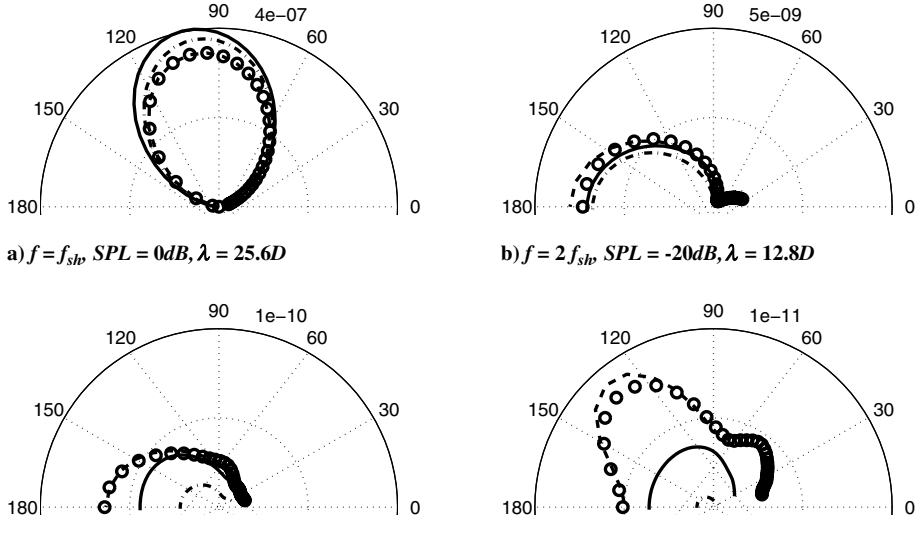

a) $f = f_{sh}$, $SPL = 0dB$, $\lambda = 25.6D$ **b) $f = 2f_{sh}$, $SPL = -20dB$, $\lambda = 12.8D$**

c) $f = 4f_{sh}$, $SPL = -37dB$, $\lambda = 6.4D$ **d) $f = 8f_{sh}$, $SPL = -49dB$, $\lambda = 3.2D$**

Fig. 10 Directivity plot of sound; solid line, hybrid approach; dashed line, directly computed sound; circle, FW-H based on compressible solution; dashed-dotted line, projection of hydrodynamic surface pressure using Eq. (6).

measurements of mean velocity in the wake of the mirror as well as wall pressure spectra on the body of the mirror and far-field sound spectra are available for validation of the computational method.

An unstructured mesh was generated for this flow configuration in which a hexahedral mesh is applied to resolve the boundary layers on the surface of the mirror as well as the surface of the test table and a combination of tetrahedral, prism, and hexahedral elements used in the rest of the domain. We homothetically refined the mesh in a zone containing the mirror and its wake. The refined mesh consists of 25×10^6 cells. After the transient flow convected out of the computational domain, we collected statistics for approximately 0.8 s of physical time. To achieve statistically converged sound, spectra of nine overlapping samples with a frequency bandwidth of 8 Hz were averaged. The nondimensional numerical time step for this calculation is $\Delta t U0/D = 4.3 \times 10^{-3}$, where L and U_0 are the mirror width and the freestream velocity, respectively. In this problem, the grid stretching close to the boundaries of the computational domain was found to be sufficient to silently damp the sound sources.

A velocity snapshot of this flow is shown in Fig. 11. Streamwise velocity contours show that the flow separates from the tip of the mirror, evolves to a turbulent shear layer, and then forms a recirculation region behind the mirror. The contour plot of wall-normal velocity, shown just above the test table, depicts the footprint of an unsteady vortex filament rolled and bent around the base of the mirror.

Figure 12 compares the LES mean velocity to the results of PIV measurements along horizontal and vertical planes cutting through the recirculation region. This result demonstrates that LES is able to accurately predict the size and shape of the recirculation region.

In Fig. 13 wall pressure spectra are plotted against nondimensionalized frequency at a pressure probe placed at the center of the mirror's flat surface. The nondimensionalized frequency can be converted to hertz by multiplying by 112. The simulation result is in agreement with the experiment for low- and midfrequency ranges (up to 0.8 kHz), but then it descends rapidly. This cutoff behavior is the natural consequence of the LES filter aiming to resolve only energy-containing scales corresponding to lower frequencies.

The sound reflects from not only the mirror but also the surface of the test table. This effect is included in the hybrid approach by using half-space acoustic Green's functions.

The sound spectrum is calculated using the hybrid approach for a microphone located 136 cm away from the mirror and is compared to experimental measurements in Fig. 14. The statistical error bars are estimated based on 95% confidence intervals based on nine samples of the spectrum. In this hybrid approach, the measured sound is followed in the frequency range of about 200 Hz to 1.5 kHz and underpredicted in the rest of the frequency range. The underprediction of sound at high frequencies is due to the limited resolution of sound sources calculated with LES, whereas at low frequencies, the inaccuracy of measured sound is largely due to the nonanechoic nature of the tunnel at corresponding frequencies. This hypothesis is further supported by a separate experiment in which a low-frequency peak corresponding to a shedding phenomenon was measured in this flow configuration [34]. This low-frequency peak is present in the LES result but not in the anechoic wind-tunnel data, most likely because the tunnel noise is high enough at low frequencies to conceal this peak.

In addition to the hybrid approach, Eq. (6) was employed to predict the sound. Similar to the case of the turbulent cylinder, this formulation yields accurate results only at low frequencies and leads to significant underprediction of sound at frequencies higher than 1 kHz. In the present calculation, the improvement gained from

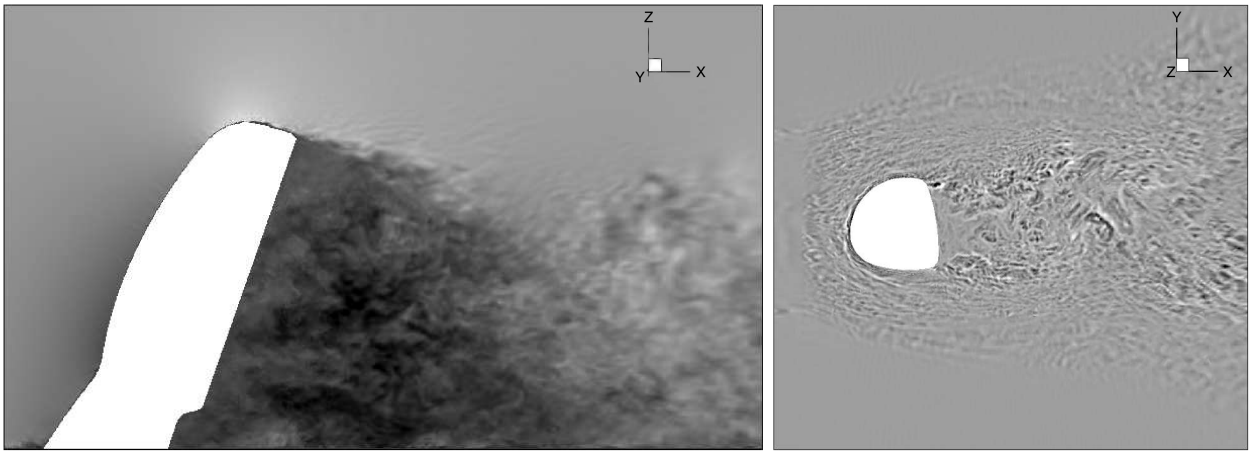

Fig. 11 Shown are the following: a) instantaneous streamwise velocity contours in the midplane of the mirror where contour levels are from -1.79 (dark) to $1.12U_0$ (light), and b) iInstantaneous wall-normal velocity contours on a plane parallel to and 1 mm above the table where contour levels are from -0.53 (dark) to $0.37U_0$ (light).

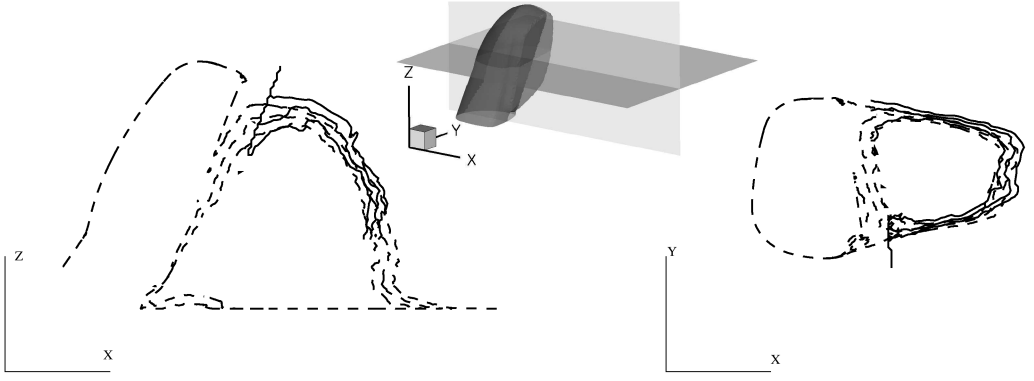

Fig. 12 Isocontours of mean streamwise velocity on two planes cutting through the recirculation region; contour levels are $\bar{u}/U_0 = -0.05, 0$, and 0.05; solid line, PIV measurements [34]; dashed line, LES calculations.

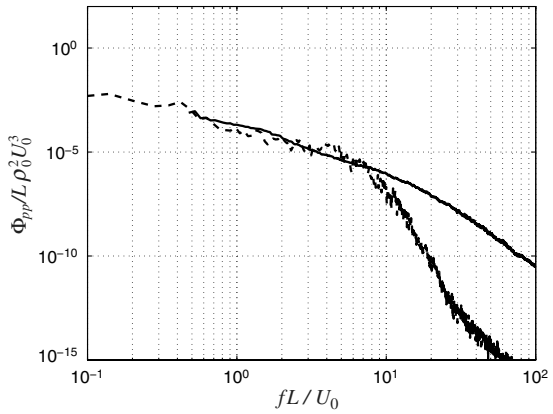

Fig. 13 Pressure spectral density for a probe located at the flat surface of the mirror; solid line, surface pressure transducer measurement [23]; dashed line, LES calculations.

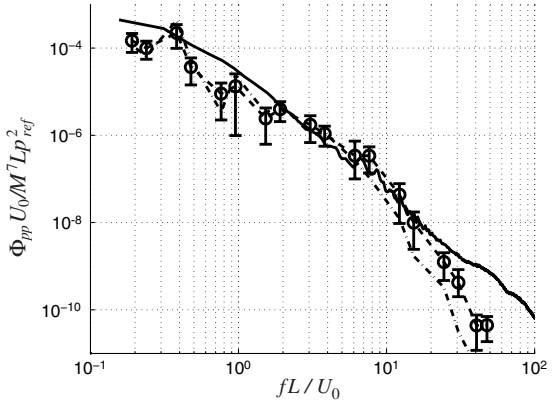

Fig. 14 Sound pressure spectra at $(x, y, z) = (0, 136, 0$ cm); solid line, anechoic wind-tunnel measurements [33]; dashed-circled line, hybrid approach; dashed-dotted line, projection of hydrodynamic surface pressure using Eq. (6).

application of the hybrid approach does not cover a wide range of frequencies. However, increased LES resolution will extend this range to higher frequencies and should highlight the difference between our approach and the approximate method in Eq. (6). We are currently applying the hybrid approach to predict the sound generated by the trailing-edge flow. In this calculation, direct numerical simulation is used to adequately resolve the high-frequency component of the sound. In these high frequencies, we expect a much larger difference between the sound predicted by the hybrid approach and the result of the approximate method.

V. Conclusions

We developed a hybrid method consisting of an incompressible flow solver and BEM to accurately predict sound generated by complex flows at low Mach numbers. This approach was validated for canonical problems of sound generated by laminar and turbulent flows over a cylinder. In laminar vortex shedding, results from this hybrid approach were successfully validated against directly computed sound as well as those from FW-H formulation. In the case of turbulent flow, we concluded that sound predicted by the hybrid method is as accurate as directly computed sound in the frequency range in which the numerical method accurately resolves the flow-generated sound sources.

As a demonstration of an engineering application, we studied the sound generated by flow over an automobile side-view mirror. The result of the hybrid approach was in good agreement with the experimental measurements in the frequency range in which the flow structures were accurately resolved by the numerical method.

Appendix: Derivation of Boundary Integral Equation in the Hybrid Approach

Equation (3) is subject to hard-wall boundary conditions on solid walls $\partial\Omega$ and the Sommerfeld condition in the far field. These conditions are written as

$$u_i n_i = 0 \quad \text{on } \partial\Omega$$
$$\lim_{r\to\infty} r^{(d-1)/2}\left(ik\tilde{p}'_a + \frac{\partial \tilde{p}'_a}{\partial r}\right) = 0 \quad \text{in far field} \tag{A1}$$

where r is the distance of sound waves from sound sources and d is the spatial dimension of the problem.

Similar to the procedure followed by Wu and Li [19], Eq. (3) is first multiplied by the adjoint Green's function of the convective Helmholtz operator appearing in the left-hand side of Eq. (3); this Green's function is denoted by $G^\dagger$. Then, we take the volume integral of this equation. This integral is carried out in Ω, which is the exterior domain enclosed by the solid boundary $\partial\Omega$ and S_r, a d dimensional large sphere with radius r centered at sound sources. Given that $\tilde{p}_a$ and $G^\dagger$ are twice continuously differentiable in Ω and $\Omega\backslash\{\mathbf{x}\}$, respectively, we using the integration by parts twice to obtain

$$\begin{aligned}
&\int_{\partial\Omega\backslash\{\mathbf{x}\}} \tilde{p}'_a \underbrace{\left(\left(ik + M_i\frac{\partial}{\partial y_i}\right)^2 - \frac{\partial}{\partial y_j\partial y_j}\right)G^\dagger}_{=0}\, \mathrm{d}\mathbf{y} \\
&\quad + \int_{\partial\Omega+S_r+S_\epsilon} (\delta_{ij} - M_iM_j)\tilde{p}'_a n_j \frac{\partial G}{\partial y_i}\, \mathrm{d}s_\mathbf{y} \\
&\quad + \int_{\partial\Omega+S_r+S_\epsilon} \left(2ikM_j\tilde{p}'_a - (\delta_{ij} - M_iM_j)\frac{\partial \tilde{p}'_a}{\partial y_i}\right)n_j G\, \mathrm{d}s_\mathbf{y} \\
&\quad = \underbrace{\int_{\partial\Omega\backslash\{\mathbf{x}\}} \frac{\partial^2 T'_{ij}}{\partial y_i\partial y_j} G\, \mathrm{d}\mathbf{y}}_{A}
\end{aligned} \tag{A2}$$

Equation (A2) is obtained using the reciprocity for the free-space Green's function, that is, $G^\dagger(\mathbf{y}|\mathbf{x}) = G(\mathbf{x}|\mathbf{y})$. In Eq. (A2), S_ϵ is an infinitesimal sphere with radius ϵ centered at $\mathbf{x}$. Applying the integration by parts to the volume integral (A) in Eq. (A2) yields

$$\begin{aligned}
&\underbrace{\int_{\partial\Omega+S_r+S_\epsilon} \left((\delta_{ij} - M_iM_j)\tilde{p}'_a + T'_{ij}\right)n_j\frac{\partial G}{\partial y_j}\, \mathrm{d}s_\mathbf{y}}_{B} \\
&\quad + \underbrace{\int_{\partial\Omega+S_r+S_\epsilon} \left(2ikM_j\tilde{p}'_a - (\delta_{ij} - M_iM_j)\frac{\partial \tilde{p}'_a}{\partial y_i} - \overbrace{\frac{\partial \tilde{T}'_{ij}}{\partial y_i}}^{=i\omega\rho u_j}\right)n_j G\, \mathrm{d}s_\mathbf{y}}_{C} \\
&\quad = \int_{\Omega\backslash\{\mathbf{x}\}} T'_{ij}\frac{\partial^2 G}{\partial y_i\partial y_j}\, \mathrm{d}\mathbf{y}
\end{aligned} \tag{A3}$$

Using the continuity and momentum equations, the expression in integral (C) is simplified to a mass flux term. Furthermore, due to the causality condition, the contribution of the far-field boundary, S_r, in integrals (B) and (C) vanishes (see Appendix B of [19]). The singular surface integral on S_ϵ vanishes in (C) due to the low-order singularity in G, but returns a finite value in (B). Thus, Eq. (A3) is written as

$$\begin{aligned}
&[\alpha A_{ij}((\delta_{ij} - M_iM_j)\tilde{p}'_a + T'_{ij})]_\mathbf{x} \\
&\quad = -\int_{\partial\Omega} ((\delta_{ij} - M_iM_j)\tilde{p}'_a + T'_{ij})n_j\frac{\partial G}{\partial y_i}\, \mathrm{d}s_\mathbf{y} \\
&\quad - \underbrace{\int_{\partial\Omega} i\omega\widetilde{\rho u_n} G\, \mathrm{d}S_\mathbf{y}}_{=0(\text{solid walls})} + \int_{\Omega\backslash\{\mathbf{x}\}} T'_{ij}\frac{\partial^2 G}{\partial y_i\partial y_j}\, \mathrm{d}\mathbf{y}
\end{aligned} \tag{A4}$$

where α is a geometrical factor defined as

$$\alpha(\mathbf{x}) = \begin{cases} 1 & \mathbf{x} \in \Omega \\ 1/2 & \mathbf{x} \in \partial\Omega \\ 0 & \text{otherwise} \end{cases} \tag{A5}$$

and A_{ij} is a diagonal matrix. Assuming the freestream velocity is in the x_1 direction ($M_i = M\delta_{i1}$) for 2-D wave propagation, the diagonal elements of A_{ij} are

$$A_{11} = \frac{\gamma^2}{\gamma+1}, \qquad A_{22} = \frac{\gamma}{\gamma^2+1} \tag{A6}$$

where $\gamma = 1/\sqrt{1-M^2}$ is the Prandtl–Glauert factor. For 3-D problems, the diagonal elements of A_{ij} are

$$A_{11} = \frac{\gamma^3}{2(\gamma^2-1)^{3/2}}\left(\ell_n \frac{\gamma+\sqrt{\gamma^2-1}}{\gamma-\sqrt{\gamma^2-1}} - 2\frac{\sqrt{\gamma^2-1}}{\gamma}\right) \tag{A7}$$

$$A_{22} = A_{33} = \frac{\gamma}{4(\gamma^2-1)^{3/2}}\left(-\ell_n \frac{\gamma+\sqrt{\gamma^2-1}}{\gamma-\sqrt{\gamma^2-1}} + 2\gamma\sqrt{\gamma^2-1}\right) \tag{A8}$$

For both 2- and 3-D problems, one also can show

$$A_{ij}(\delta_{ij} - M_i M_j) = 1 \tag{A9}$$

and for a small Mach number the diagonal elements can be well approximated using

$$A_{ij} = (1/d + O(M^2))\delta_{ij} \tag{A10}$$

By substituting Eq. (A9) into Eq. (A4), we arrive at the following boundary integral equation employed in the hybrid approach:

$$[\alpha((\tilde{p}'_a + A_{ij}T'_{ij})]_{\mathbf{x}} = -\int_{\partial\Omega}((\delta_{ij} - M_i M_j)\tilde{p}'_a + T'_{ij})n_j \frac{\partial G}{\partial y_i}\, \mathrm{d}s_{\mathbf{y}} + \int_{\Omega\setminus\{\mathbf{x}\}} T'_{ij}\frac{\partial^2 G}{\partial y_i \partial y_j}\, \mathrm{d}\mathbf{y} \tag{A11}$$

where Green's function is the free-space Green's function of the convective Helmholtz operator. Assuming $M_i = M\delta_{i1}$ and using the Prandtl–Glauert transformation, G can be calculated from the free-space Green's function of the ordinary Helmholtz operator denoted by G^0 as follows:

$$G(\mathbf{x}|\mathbf{y}, k) = \gamma e^{iMk\gamma(x'_1 - y'_1)} G^0(\mathbf{x}'|\mathbf{y}', k') \tag{A12}$$

where $x'_1 = \gamma x_1$, $y'_1 = \gamma y_1$, and $k' = \gamma^2 k$. For detailed derivations of the relations presented in this Appendix, see [35].

Acknowledgments

This work was supported by the Office of Naval Research, the U.S. Department of Energy under the Advanced Simulation and Computing program, and General Motors Corporation. The authors are indebted to M. Wang and D. Bodony for their invaluable suggestions during the course of this project. The sound and surface pressure measurements were carried out by S. Morris and D. Shannon in the anechoic chamber facility at Hessert Laboratory for Aerospace Research at the University of Notre Dame. The authors are grateful to G. Iaccarino for providing the computational grid for the side-view mirror case.

References

[1] Lighthill, M. J., "On Sound Generated Aerodynamically. I. General Theory," *Philosophical Transactions of the Royal Society of London, Series A: Mathematical and Physical Sciences*, Vol. 211, 1952, pp. 564–587. doi:10.1098/rspa.1952.0060

[2] Curle, N., "The Influence of Solid Boundaries Upon Aerodynamic Sound," *Philosophical Transactions of the Royal Society of London, Series A: Mathematical and Physical Sciences*, Vol. 231, 1955, pp. 505–514. doi:10.1098/rspa.1955.0191

[3] Wang, M., andMoin, P., "Computation of Trailing Edge Flow and Noise Using Large-Eddy Simulation," *AIAA Journal*, Vol. 38, 2000, pp. 2201–2209. doi:10.2514/2.895

[4] Marsden, A. L., Wang, M., Dennis, J. E., and Moin, P., "Trailing Edge Noise Reduction Using Derivative-Free Optimization and Large-Eddy Simulation," *Journal of Fluid Mechanics*, Vol. 572, 2007, pp. 13–36. doi:10.1017/S0022112006003235

[5] Wang, M., Moreau, S., Iaccarino, G., and Roger, M., "LES Prediction of Wall-Pressure Fluctuations and Noise of a Low-Speed Airfoil," *International Journal of Aeroacoustics*, Vol. 8, No. 3, 2009, pp. 177–198. doi:10.1260/147547208786940017

[6] Ffowcs Williams, J. E., and Hall, L. H., "Aerodynamic Sound Generation by Turbulent Flow in the Vicinity of a Scattered Half Plane," *Journal of Fluid Mechanics*, Vol. 40, 1970, pp. 657–670. doi:10.1017/S0022112070000368

[7] Howe, M. S., "Edge-Source Acoustic Greens Function for an Airfoil of Arbitrary Chord, with Application to Trailing-Edge Noise," *Quarterly Journal of Mechanics and Applied Mathematics*, Vol. 54, 2001, pp. 139–155. doi:10.1093/qjmam/54.1.139

[8] Manoha, E., Elias, G., Troff, B., and Sagaut, P., "Towards the Use of Boundary Element Method in Computational Aeroacoustics," *5th CEAS/AIAA Aeroacoustics Conference*, AIAA, Reston, VA, 1999, pp. 1161–1171; also AIAA Paper 99-1980.

[9] Ostertag, J. S. D., Celic, A., and Wagner, S., "Trailing-Edge Noise Prediction by SATIN on the Basis of Steady RANS Solutions," AIAA Paper 2002-2471, 2002.

[10] Hu, F. Q., Guo, Y. P., and Jones, A. D., "On the Computation and Application of Exact Greens Function in Acoustic Analogy," AIAA Paper 2005-2986, 2005.

[11] Oberai, A. A., Roknaldin, F., and Hughes, T., "Computation of Trailing Edge Noise Due to Turbulent Flow over an Airfoil," *AIAA Journal*, Vol. 40, 2002, pp. 2206–2216. doi:10.2514/2.1582

[12] Keller, J., and Givoli, D., "Exact Non-Reflecting Boundary Conditions," *Journal of Computational Physics*, Vol. 82, 1989, pp. 172–192. doi:10.1016/0021-9991(89)90041-7

[13] Bérenger, J., "A Perfectly Matched Layer for the Absorption of Electromagnetic Waves," *Journal of Computational Physics*, Vol. 114, 1994, pp. 185–200. doi:10.1006/jcph.1994.1159

[14] Astley, R. J., "Infinite Elements for Wave Problems: A Review of Current Formulations and an Assessment of Accuracy," *International Journal for Numerical Methods in Engineering*, Vol. 49, 2000, pp. 951–976. doi:10.1002/1097-0207(20001110)49:7<951::AID-NME989>3.0.CO;2-T

[15] Ham, F., and Iaccarino, G., "Energy Conservation in Collocated Discretization Schemes on Unstructured Meshes," *Center for Turbulence Research Annual Research Briefs*, Stanford Univ./NASA, Stanford, CA, 2004, pp. 3–14.

[16] Khalighi, Y., and Bodony, D., "Improved Near-Wall Accuracy for Solutions of the Helmholtz Equation Using the Boundary Element Method," *Center for Turbulence Research Annual Research Briefs*, Stanford Univ./NASA, Stanford, CA, 2006, pp. 313–322.

[17] Crow, S. C., "Aerodynamic Sound Generation as a Singular Perturbation Problem," *Studies in Applied Mathematics*, Vol. 49, 1970, pp. 21–44.

[18] Schram, C., "A Boundary Element Extension of Curles Analogy for Non-Compact Geometries at Low-Mach Numbers," *Journal of Sound and Vibration*, Vol. 322, No. 1-2, 2009, pp. 264–281. doi:10.1016/j.jsv.2008.11.011

[19] Wu, T. W., and Li, L., "A New Boundary Integral Formulation for Acoustic Radiation in a Subsonic Uniform Flow," *Journal of Sound and Vibration*, Vol. 175, No. 1, 1994, pp. 51–63. doi:10.1006/jsvi.1994.1310

[20] Astley, R. J., and Bain, J. G., "A Three-Dimensional Boundary Element Scheme for Acoustic Radiation in Low Mach Number Flows," *Journal of Sound and Vibration*, Vol. 109, No. 3, 1986, pp. 445–465. doi:10.1016/S0022-460X(86)80381-9

[21] Crighton, D. G., "Computational Aeroacoustics for Low Mach Number Flows," *Computational Aeroacoustics*, Springer–Verlag, Berlin/New York/Heidelberg, 1993, pp. 50–68.

[22] Shariff, K., and Wang, M., "A Numerical Experiment to Determine Whether Surface Shear-stress Fluctuations Are a True Sound Source,"

Physics of Fluids, Vol. 17, 2005, pp. 107105.
doi:10.1063/1.2112747

[23] Ham, F., Mattsson, K., Iaccarino, G., and Moin, P., *Towards Time-Stable and Accurate LES on Unstructured Grids*, Vol. 56, Lecture Notes in Computational Science and Engineering, Springer, New York, 2007, pp. 235–249.

[24] Schenck, H. A., "Improved Integral Formulation for Acoustic Radiation Problems," *Journal of the Acoustical Society of America*, Vol. 44, 1968, pp. 41–58.
doi:10.1121/1.1911085

[25] Li, X., and Demmel, J., "SuperLUDIST: A Scalable Distributed-Memory Sparse Direct Solver for Unsymmetric Linear Systems," *ACM Transactions on Mathematical Software*, Vol. 29, 2003, pp. 110–140.
doi:10.1145/779359.779361

[26] Morfey, C. L., "The Role of Viscosity in Aerodynamic Sound Generation," *International Journal of Aeroacoustics*, Vol. 2, Nos. 3–4, 2003, pp. 225–240.
doi:10.1260/147547203322986124

[27] Ffowcs Williams, J. E., and Hawkings, D. L., "Sound Generation by Turbulence and Surfaces in Arbitrary Motion," *Philosophical Transactions of the Royal Society of London, Series A: Mathematical and Physical Sciences*, Vol. 264, May 1969, pp. 321–342.
doi:10.1098/rsta.1969.0031

[28] Nagarajan, S., Lele, S., and Ferziger, J., "A Robust High-Order Compact Method for Large Eddy Simulation," *Journal of Computational Physics*, Vol. 191, 2003, pp. 392–419.
doi:10.1016/S0021-9991(03)00322-X

[29] Fey, U., König, M., and Eckelmann, H., "A New Strouhal–Reynolds-Number Relationship for the Circular Cylinder in the Range $47 < Re < 2 \times 10^5$," *Physics of Fluids*, Vol. 10, No. 7, 1998, pp. 1547–1549.
doi:10.1063/1.869675

[30] Wang, M., Lele, S., and Moin, P., "Computation of Quadrupole Noise Using Acoustic Analogy," *AIAA Journal*, Vol. 34, 1996, pp. 2247–2254.
doi:10.2514/3.13387

[31] Bodony, D., "Analysis of Sponge Zones for Computational Fluid Mechanics," *Journal of Computational Physics*, Vol. 212, 2006, pp. 681–702.
doi:10.1016/j.jcp.2005.07.014

[32] Germano, M., Piomelli, U., Moin, P., and Cabot, W., "A Dynamic Subgrid-Scale Eddy Viscosity Model," *Physics of Fluids*, Vol. 3, No. 7, 1991, pp. 1760–1765.

[33] Morris, S. C., and Shannon, D. W., "Experimental Measurements of Sound Generated by Automobile Side-View Mirrors," Hessert Laboratory for Aerospace Research, Univ. of Notre Dame, Tech. Rept. UND-SM07-330, Notre Dame, IN, Dec. 2007.

[34] Johnson, J. and Khalighi, B., "Experimental Characterization of the Unsteady Flow Field Behind Automobile Side-View Mirrors," Institute for Aerospace Research at the National Research Consortium Canada and General Motors Corporation, Dec. 2005.

[35] Khalighi, Y., "Computational Aeroacoustics of Complex Flows at Low Mach Number," Ph.D. Thesis, Stanford Univ., Stanford, CA, 2009.

J. Astley
Associate Editor